



Diana Stellmach, Fanxing Xi, Ulrike Bloeck, Peter Bogdanoff*
and Sebastian Fiechter*

Catalytic Behavior of Molybdenum Sulfide for the Hydrogen Evolution Reaction as a Function of Crystallinity and Particle Size Using Carbon Multiwall Nanotubes as Substrates

<https://doi.org/10.1515/zpch-2019-1490>

Received May 31, 2019; accepted February 10, 2020

Abstract: Molybdenum sulfide is of interest as a noble metal-free catalyst for the hydrogen evolution reaction (HER). In crystallized form, it shows a typical stacking of planar S–Mo–S layers whereas the catalytically active centers are situated on the edges of these entities characterized by non-saturated bonds of the molybdenum atoms. In this study, 2H-MoS₂ is investigated as HER catalyst as a function of particle size using powder electrodes of different grain sizes and morphology. HER was also determined as a function of growth defects (bending of layers) and as a function of active sites employing MoS₂ nanoparticles (NP). To study the influence of the substrate on the perfection of the transition metal disulfide, MoS₂ nanosheets were deposited on multi-walled carbon nanotubes (MWCNTs) of different diameters. Highest activity was found for MoS₂ nanosheets deposited on MWCNTs with a diameter smaller than 8 nm. At diameters larger than 10 nm, a wrapping of the nanotubes by partially bended stacks of S–Mo–S layers occurs, while at diameters smaller than 10 nm, individual MoS₂ nanosheets of 3–5 S–Mo–S stacks of 3–4 nm in height and 10–20 nm in lateral extension surround the carbon nanotubes in form of hexagonal cylinders. The ratio of catalytically active non-van-der-Waals and hexagonal basal planes was determined electrochemically by electro-oxidation and correlated with HER activity.

Keywords: electro-oxidation; hydrogen evolution catalyst; molybdenum sulfide; multi wall carbon nanotubes; Raman spectra; reactive center.

***Corresponding authors: Peter Bogdanoff and Sebastian Fiechter,** Helmholtz-Zentrum Berlin für Materialien und Energie GmbH, Institute Solar Fuels, 14109 Berlin, Germany, e-mail: bogdanoff@helmholtz-berlin.de (P. Bogdanoff); fiechter@helmholtz-berlin.de (S. Fiechter)

Diana Stellmach and Fanxing Xi: Helmholtz-Zentrum Berlin für Materialien und Energie GmbH, Institute Solar Fuels, 14109 Berlin, Germany

Ulrike Bloeck: Department of Structure and Dynamics of Energy Materials, Helmholtz-Zentrum Berlin für Materialien und Energie, 14109 Berlin, Germany

1 Introduction

Molybdenum disulfide can be used for different applications because of its highly anisotropic layer structure. It is used as a catalyst for the hydrodesulfurization process of crude oil [1], as transistor material using its semiconducting phase [2], but also as a solid lubricant [3]. It occurs in three different layer-type crystal structures, namely 2H-MoS₂, 3R-MoS₂ and 1T-MoS₂. Among them, 2H and 3R are the two main phases whereas the 2H phase is the dominant and most stable phase in nature. As shown in Figure 1, 2H-MoS₂ contains two S–Mo–S layer sequences per unit cell with a trigonal prismatic coordination of the molybdenum atoms by sulfur, while the unit cell of 3R-MoS₂ comprises three layer sequences [4]. The 1T-MoS₂ phase is characterized by an octahedral coordination of molybdenum by sulfur leading to a metallic property [5, 6]. Bulk 2H-MoS₂ is a compound semiconductor having an indirect band gap of 1.29 eV and a direct one of 1.8 eV, which is depending on the number of van der Waals layers in MoS₂ [7].

Among the non-precious metal catalysts that have been studied, molybdenum disulfide has stood out for its high catalytic activity of the HER and its high stability, especially under acidic conditions. Interestingly in former studies, MoS₂ was thought to only have low catalytic ability for HER [8]. However, according to theoretical calculations, the material should be relatively active for HER since it exhibits modest binding energies with atomic hydrogen and relatively high exchange current density as shown by Jaramillo et al. [9]. In the same paper, the authors describe that the exchange current density of the material is proportional to the edge length of a MoS₂ electrode. Therefore, the catalytically active sites of MoS₂ are found to be located on the edge site of the hexagonal layers.

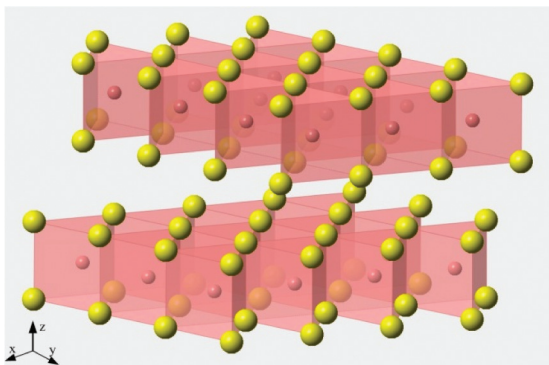


Fig. 1: Crystal structure of hexagonal MoS₂ crystallizing in the space group P6₃/mmc.

Since then, researchers have put a lot effort to increase the catalytic ability of MoS₂ for HER. One strategy to increase the catalytic activity is simply generating more active sites at the catalyst surface. To achieve this goal, Kibsgaard et al. [10] in 2012 engineered the surface structure of mesoporous MoS₂ thin films with a high degree of surface curvature to preferentially expose more edge sites than basal planes, leading to improved catalytic properties. Using high temperature hydrogen annealing, Kiriya et al. [11] discovered that the catalytic ability of different molybdenum sulfides, for instance, bulk, powder and nanoflakes of MoS₂, can be increased because of a higher surface area and more active sites due to thermal texturization. In 2016, Li et al. [12] increased the active site number by introducing and straining sulfur vacancies to activate the basal plane of MoS₂. DFT calculation suggested higher hydrogen adsorption and optimal Gibbs free energy of hydrogen adsorption (ΔG_{H^*}) in the strained, S-vacancy activated MoS₂ catalyst, leading to a lower overpotential (170 mV at 10 mA/cm²).

Other than modifying the structure of MoS₂ itself, molybdenum sulfides with different structures were also studied. For example, cluster-type molybdenum sulfides with a large number of edge atoms per unit area are expected to be a hydrogen evolution catalyst (HEC) of high performance. The incomplete cubane-typed [Mo₃S₄]²⁻ cluster was used as HEC in 2008 by Jaramillo et al. The [Mo₃S₄]²⁻ cluster obtained a similar overpotential compared with MoS₂ NPs of about 300 mV at -10 mA/cm² [13]. Then in 2014, the thiomolybdate cluster [Mo₃S₁₃]²⁻ was described as an efficient HER catalyst with a high number of sulfur atoms located at the edges of the cluster units exhibiting an overpotential of 180 mV at -10 mA/cm² and high stability (10–20 mV increase of overpotential at 10 mA/cm² after 1000 cycles of cyclic voltammetry in the potential range from 0.2 to -0.3 V with a 100 mV/s scan rate) [14].

Besides, amorphous MoS_x was also discovered for its excellent catalytic activity. The amorphous MoS_x has a different structure other than layer structured MoS₂ which gave the material an unique catalytic behavior. Amorphous MoS_x can be synthesized through electrodeposition [15], wet chemical reaction [16], and sulfurization without thermal treatment [17, 18]. The origin of the high catalytic performance of amorphous MoS_x was not clear for a long time. The high surface area [19] and the existence of bridging and terminal [S₂]²⁻ were thought to be possible reasons [16]. In 2016, Yeo et al. [20] found that the composition of S species in amorphous MoS_x was changed during HER. In the meantime, Artero et al. [21] observed loss of terminal [S₂]²⁻ during HER condition, also suggesting that MoS_x went through structural changes in HER catalysis process. In the previous study of our group [22], the structural transformation of amorphous MoS_x from a [Mo₃S₁₃]²⁻ cluster-like material to a MoS_{2-x} layer-type material was identified.

There are still other methods to improve the catalytic ability of molybdenum sulfide. Literatures have already shown that doping MoS_x with elements such as Co, Fe and Ni could improve its catalytic ability [19]. Besides, by electrochemical exfoliation, the thermodynamically favored 2H- MoS_2 can be partially transformed to a 1T polymorph which has more metallic character and more competitive HER activity [23]. However, even though much progress has been achieved during the past, the catalytic performance of MoS_2 as HER catalyst, in both activity and stability, is still much inferior to that of platinum and the catalytic mechanism of MoS_2 is partially not yet understood. For this reason, efforts still need to be made for further improvement of its catalytic ability and a detailed understanding of its catalytic mechanism.

In this paper, we compare MoS_2 powders of different grain size with MoS_2 nanosheets deposited on multi-walled carbon nanotubes (MWCNTs). Owing to two oxidation peaks found in cyclic voltammetry (CV) measurements electro-oxidizing MoS_2 , the area of catalytically active edges of the hexagonal material in contact with the electrolyte can be determined and compared with the areas of the chemically inert basal planes. Using the surfactant Tween 80, which reacts with unsaturated metal ions located at the layer edges and therefore blocks the active centers, the first oxidation peak has been assigned to the oxidation of the catalytic centers. Thus, the ratio of edge to basal planes in MoS_2 can be determined by electrochemical CV measurements.

2 Experimental

2.1 MoS_2 electrodes preparation

2.1.1 MoS_2 preparation

MoS_2 single crystals, used as a reference material in this work, were grown by chemical vapor transport using MoO_3 and IBr as transporting agents. In a first step, MoS_2 (2 g) and MoO_3 powder (25 mg) were placed at the closed end of a 190 mm long and closed quartz glass tube of 20 mm diameter. Afterwards, the ampoule was evacuated and prior to sealing IBr (365 mg) was sublimed at the cooled end of the ampoule. The tube was placed into a two zone furnace. In a temperature gradient $\Delta T = 1173 - 1123$ K endothermal transport was observed from hot to cold. After 200 h, crystals up to 5–10 mm edge length were grown in the growth chamber of the ampoule. Crystals investigated in this paper as hydrogen evolving catalysts showed typical growth spirals on the basal planes which have step sizes of several hundred nanometers.

MoS₂ powder (# DS-315) was prepared by a precipitation reaction dissolving sodium molybdate and thioacetamide in an acid solution: a 10 mM thioacetamid solution dissolved in 1 M HCl was added to an aqueous 1 mM Na₂MoO₄ · 2H₂O solution. Afterwards, the mixture was stirred for 12 h and finally the molybdenum sulfide particles were filtered using a PTFE filter. The obtained product was heated in forming gas (10% H₂ in N₂) at 450 °C for 1 h before the product was heated at 800 °C for 2 h under argon gas. The powder sample (# SF) was synthesized from the elements at 500 °C in an evacuated and sealed quartz glass ampoule for 50 h by weighing-in molybdenum and sulfur in the mass ratio of 1:2. The samples Sigma Aldrich I & II (shortly SA I & II), Molykote μ-size, and Molykote z-size were purchased from Sigma Aldrich and Dow Chemicals, respectively. The preparation method of these powders is unknown and not specified by the manufacturer. Molykote powders are produced by the manufacturer as lubricants for metals. According to the data sheet, the particle size of the Molykote μ-size preparation is 0.65–0.75 μm and that of the Molykote z-powder 3–4 μm. According to the supplier the particle size was determined using the Fischer method. The preparation of the samples SA I & II is also unknown and also the method by which the particle size was determined is not described. Looking at SEM images, a high size distribution of the hexagonal platelets can be seen for all commercial samples. The particles appear to be mechanically fractured and show numerous crystallite fragments (see Figure 2). Sample DS-315 has a particle size of <200 nm, the particles of the powder #SF have a particle size ranging from 50 to 1000 nm.

MoS₂ grown on MWCNTs was prepared using the same method as described for the preparation of DS-315 powder. In an aqueous 1 mM Na₂MoO₄ · 2H₂O solution 48 mg of MWCNTs were dispersed and ultrasonically homogenized at RT. After 1 h treatment, a 10 mM thioacetamid solution dissolved in 1 M HCl was added and homogenized for 2 h in an ultrasonic bath. Afterwards, the mixture was stirred for 12 h and finally MWCNT supported molybdenum sulfide was filtered using a PTFE filter. The obtained product was in a first step heated in forming gas (10% H₂ in N₂) at 450 °C for 1 h and then at 800 °C for 2 h under argon gas (Ar).

2.1.2 Electrode preparation

Ten milligrams MoS₂ powder catalyst or MoS₂ catalyst deposited on MWCNT were mixed with 1 mL poly(3,4-ethylenedioxythiophene) polystyrene sulfonate (PEDOT: PSS), which was diluted before in water in a ratio 0.3:7. After homogenizing the dispersion in an ultrasonic bath, 10 μL of the mixture was drop-casted on a FTO substrate of 10 × 20 cm² in size. The samples were first dried in air at RT

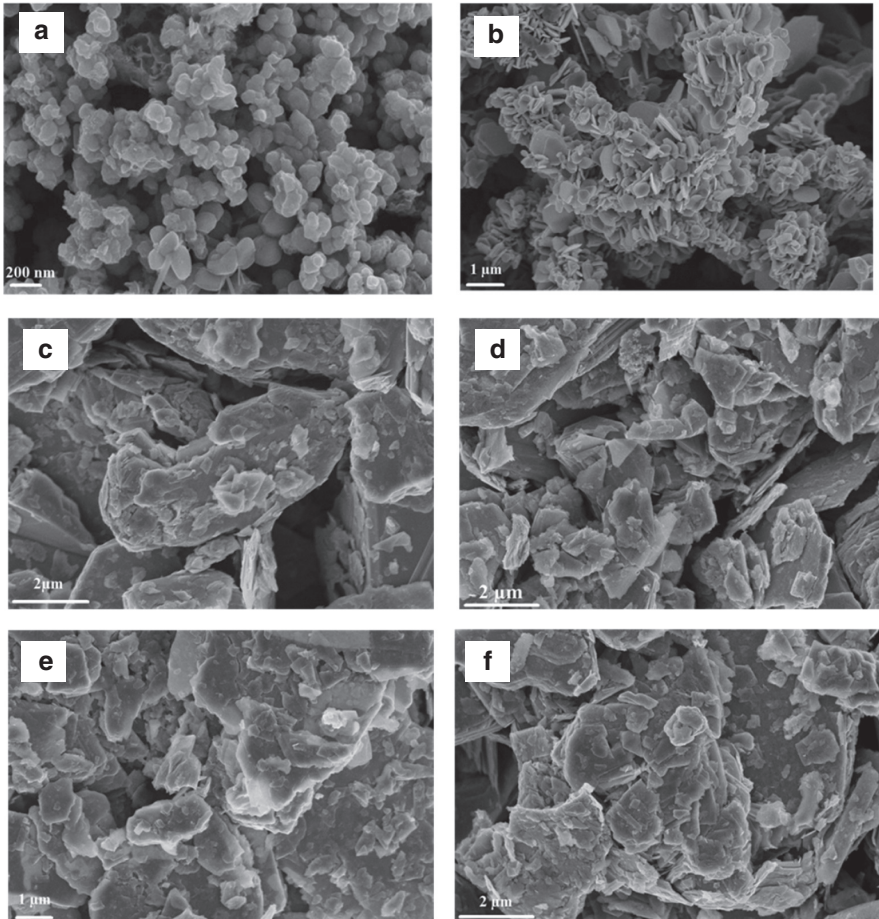


Fig. 2: SEM images of different MoS₂ powders: (a) DS-315 (<200 nm particle size), (b) SF (50 nm–1000 nm), (c) Molykote μ-size (0.65–0.75 μm), (d) Sigma Aldrich I, (e) Molykote z-powder (mean particle size 3–4 μm), and (f) Sigma Aldrich II (<8 μm).

and afterwards at 125 °C. To perform XRD measurements, the MoS₂ powders and MoS₂ deposited on MWCNTs particles were deposited on 111-oriented Si wafers.

2.2 Structural and morphological characterization

The morphology of the films was measured by field emission scanning electron microscopy (FESEM) using a LEO GEMINI 1530 instrument from ZEISS, operated with an acceleration voltage of 5 kV. For transmission electron microscopy (TEM) analysis, MoS₂ catalyst deposited on top of MWCNTs were prepared ultramicrotomically. In the first step, the MoS₂ coated nanotubes were embedded in an acrylic

resin (LR-White). Prior to cutting the small polymer blocks by ultramicrotomy (ULTRACUT E from Reichert & Jung), it was trimmed and acuminated. Ultrathin slices (40–60 nm thick) were cut from the resin tip and were floated on a water surface from where they were subsequently fixed on carbon film covered grids. Alternatively, small slices (0.5 mm thick) were cut from the tiny resin block and glued face to face. Afterwards these samples were sanded and polished perpendicular to the glued interface down to a thickness of 4–6 μm before they were fixed to a molybdenum ring. At the end the samples were ion-milled (5 kV, 2 mA) using Ar ions under an incidence angle of 6° until parts of the sample became transparent for the electron beam. Finally, the so prepared samples were investigated by a transmission electron microscope (Cm 12 from Philips, equipped with a LaB_6 cathode) and electron micrographs were taken at an acceleration voltage of 120 kV. A Bruker AXS D8 Advance X-ray diffractometer with Cu $K\alpha$ radiation ($\lambda = 0.15406$ nm) was used to obtain glancing incidence X-ray diffractiongrams (GIXRD). The angle of incidence was 0.5° and the measured detection angle (2θ) was varied from 10° to 60° . Raman spectroscopy was performed using a LabRam spectrometer from Horiba Jobin Yvon under excitation conditions using a He/Ne laser with $\lambda = 632.82$ nm, which was focused via a microscope (Olympus BX 40) on the surface of the samples. A CCD camera detected the Raman peaks.

2.3 Electrochemical measurements

Cyclic voltammetry (CV) measurements were performed using a VersaSTAT3 potentiostat in a three-electrode configuration. MoS_2 electrodes deposited on FTO were used as working electrodes (WE) while an Ag/AgCl electrode in saturated KCl solution (-0.197 V vs. reversible hydrogen electrode (RHE)) served as reference electrode (RE), and a platinum wire as counter electrode (CE). The electrolyte used was a 0.5 M H_2SO_4 aqueous solution (pH 0.3). The contacting area of the sample with the electrolyte was fixed using an O-ring of 0.63 cm diameter which is equivalent to an electrode area of 0.3117 cm^2 . The iR drop of the sample in the electrolyte was calculated by measuring the resistance of the sample in the electrolyte at 100 kHz using electrochemical impedance spectroscopy (EIS). The current density was evaluated from cyclic voltammetry (CV) measurements. The CV measurements were performed within the potential range from 0.6 V to -0.4 V vs. RHE with a scan rate of 10 mV/s. The double layer capacitance (C_{dl}) of the CV curves shown in Figure 4 and Figure 8 were extracted calculating $\Delta j = j_a - j_c$ (j_a and j_c represent anodic and cathodic current densities) at a potential $U = 0$ V using the equation $j_a - j_c = C_{dl} dU/dt$. The obtained value was added to the j_c -V curves. The corrected curves are shown in the Figures S2 and S3 of the Supplementary information. The edge sites of the MoS_2 nanoparticles were catalytically

passivated by immersing the electrodes in 5 m% Tween80 solution for 2 days under continuous stirring.

3 Results and discussion

3.1 MoS₂ powder electrodes

Six kinds of MoS₂ powders were compared with each other with respect to their HER activity. The morphology of the electrodes prepared from different MoS₂ powders is shown in the SEM images of Figure 2. According to the morphology, sample DS-315 has the smallest and most isotropic particle sizes ranging from 100 to 200 nm (Figure 2a). The typical platelet-like hexagonal growth features of 2H-MoS₂ occur in the powder sample #SF (Figure 2b). The other four commercial samples (Figure 2c–e) have a totally different morphology. Their shapes point at fractured hexagonal platelets with 1–10 μm extension of the (001) facets. Therefore, it is difficult to predict which of these samples has the highest fraction of small MoS₂ fragments.

According to the XRD patterns in Figure 3a, all six powders show the typical diffraction pattern of 2H-MoS₂. However, sample DS-315 also shows peaks of MoO₂ which could be from the residual reactant sodium molybdate (Na₂MoO₄). The increasing intensity of the 00.2 diffraction peak at 14.4 °C in the XRD patterns represents an increasing crystallinity. Sample DS-315 has the lowest peak intensity and highest full width half maximum (FWHM), which means that the sample

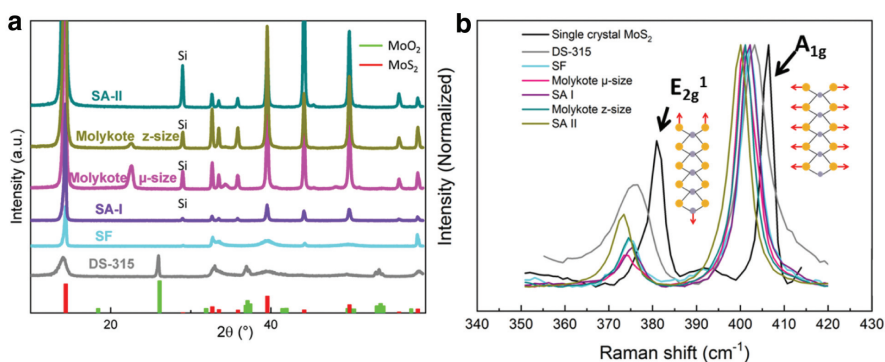


Fig. 3: (a) XRD patterns of MoS₂ powders with standard 2H-MoS₂ pattern (red) and MoO₂ pattern (green) displayed at the bottom of the figure; (b) Raman spectra of different MoS₂ powders including commercial products (Sigma Aldrich I (SA I), Sigma Aldrich II (SA II), Molykote z-size, Molykote μ-size), MoS₂ prepared by precipitation (DS-315), and chemical synthesis under vacuum (SF), in relation to a MoS₂ single crystal. In addition, schemes for the vibrational modes (E_{2g}^1 and A_{1g}) of hexagonal MoS₂ are shown.

has lower crystallinity and smaller particle sizes as compared to the other five samples.

In addition, the 00.2 peak is slightly shifted to a smaller 2θ -value of about 0.35° indicating an increased distance between the S–Mo–S layers unities due to a disturbed stacking of the S–Mo–S slabs. The 10.1 peak appears to be shifted to a higher 2θ -value pointing at a smaller a_0 lattice constant possibly caused by sulfur point defects. Using Scherrer's equation, coherently scattering crystallites of about 7 nm in height were determined from the broadening of the 00.2 peak which relates to about twelve S–Mo–S stacks.

Figure 3b shows the Raman spectra of the MoS₂ powders. In this figure, a MoS₂ single crystal was used as reference material. Its Raman spectrum shows strong characteristic peaks at 382 cm^{-1} due to in-plane vibration of Mo–S bonding in the layer structure of 2H-MoS₂, namely E_{2g}^1 mode and at 407 cm^{-1} owing to an out of plane vibration of the S–S bonding, which could be assigned as A_{1g} mode (see scheme in Figure 3b) [24–26]. All powder samples show a red shift of the E_{2g}^1 peak by 8 cm^{-1} and of the A_{1g} mode by 7 cm^{-1} and additional broadening of the peaks. In general, the peak shift and broadening of the Raman peaks could be affected by different factors, such as crystallite size [27], numbers of stacked S–Mo–S layer entities or extension of the van-der-Waals surface area [28], strain in the layers [29], changes in composition [30], and degree of oxidation [31].

CV measurements were used to investigate the electrochemical activity of the MoS₂ powders. Figure 4a shows the CV curves of the powder electrodes. The sample DS-315, which has the smallest particle size according to the morphology shown in Figure 2a, exhibited the highest current density (1 mA cm^{-2} at a potential of -0.3 V vs. RHE) owing to small areas of the (00.1) basal planes but a large number of sulfur determined edges ((hk.0) facets). Interestingly, the catalytic

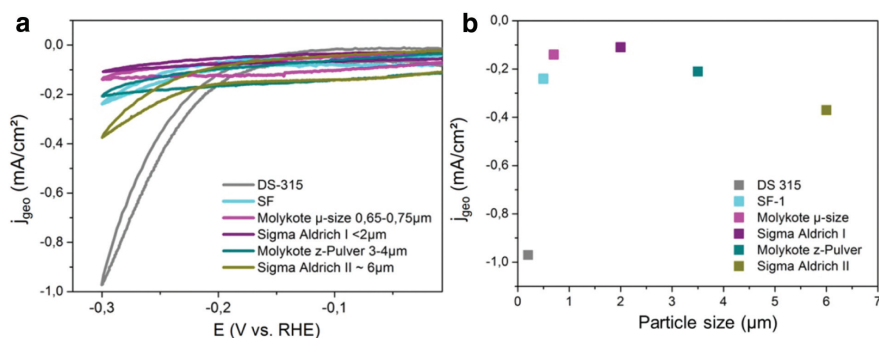


Fig. 4: (a) CV curves of the MoS₂ powder electrodes; measured in 0.5 M H₂SO₄ at a scan rate of 10 mV/s; the data were iR-corrected according to the procedure described in the experimental section; for C_{dl} corrected curves see Figure S2; (b) dependence of the current density at -0.3 V vs. RHE on particle size, the data were taken from Figure 4 (a).

activity of sample #SF is worse than that of the commercial powder SA II, indicating that the number of active sites in sample SA II is higher although its mean particle size is much larger. This effect could be explained by a high number of smaller fragments in this sample which is underestimated in the particle size determination from Figure 2f. Figure 4b shows the current density of different electrodes at the reversal point of the potential scan at -0.3 V vs. RHE as a function of particle size of the MoS_2 powder. At this highest applied potential the Faraday current has the largest contribution to the measured total current, so that it is the most suitable point for a comparison of the HER activity. It should be noted, however, that these data also include a certain amount of capacitive effects (see corrected curves in Figures S2 and S3). The current density of the electrode increases strongly as soon as the particle size becomes smaller than $1 \mu\text{m}$. This result is in consistent with the fact that only the edge sites of MoS_2 layers are catalytically active.

3.2 MoS_2 deposited on MWCNTs

In order to further increase the area of non-van-der-Waals planes where the catalytically active centers are located, MoS_2 nanosheets were grown by the precipitation reaction described above on MWCNT substrates of different diameters. Four different series of samples were produced varying the MWCNT diameter from <8 nm to ≥ 50 nm. The diameters of the MWCNTs used as substrates for MoS_2 nanosheets, namely ARKM00x, are shown in Table 1.

The MoS_2 samples deposited on MWCNTs were compared with the DS-315 powder sample prepared by the same protocol. According to the XRD patterns in Figure 5, they all show both the 00.2-reflection and the representative reflections of (hk.0) and (h0.l) lattice planes as well. The (hk.0) reflections referred to lattice planes parallel to the c-axis of related crystallites. In case of (h0.l) reflections, the planes intersect the a_0 - as well as the c_0 -axis. In addition to the characteristics of MoS_2 , the XRD patterns also exhibit peaks belonging to MoO_2 . The presence of this phase can be explained by residual reactant sodium molybdate (Na_2MoO_4) in the

Tab. 1: The diameters of MWCNTs used as carriers for MoS_2 .

MWCNT	Diameter (nm)
ARKM001	<8
ARKM002	10–20
ARKM004	40–50
ARKM005	>50

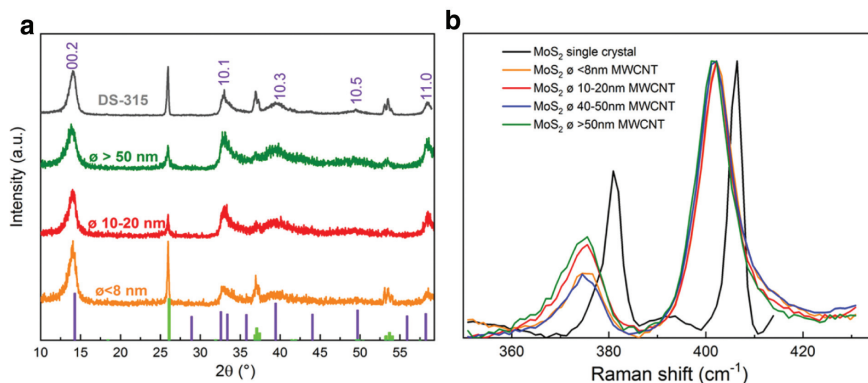


Fig. 5: (a) XRD of MoS₂ layers on MWCNTs with various tube diameters: ARKM001 $\phi < 8$ nm, ARKM002 $\phi 10\text{--}20$ nm, ARKM005 $\phi > 50$ nm. Standard patterns of 2H-MoS₂ (purple) and MoO₂ (green) are shown on the bottom of the graph; (b) Raman spectra of MoS₂ nanosheets deposited on MWCNTs, compared with MoS₂ single crystal.

batch or by a partial oxidation of the nanosheets in contact with air. Figure 5b displays the corresponding Raman spectra of MoS₂ deposited on different MWCNTs. All samples show the MoS₂ typical vibrational modes, which could be addressed as E_{2g}¹ and A_{1g}. Compared with the Raman spectrum of a MoS₂ single crystal they are red shifted and show a broadening of the peaks indicating structural defects, partial oxidation or deviations from stoichiometry as also discussed in Figure 3b [27, 29, 31–34]. In Figure S1 of the supporting information, the Raman spectra of the MWCNT supports are also shown. From the spectra it can be concluded that the most perfect nanotubes had a diameter ≤ 8 nm [35, 36]. As explained in the following, structural nanotube perfection presumably does indirectly influence the performance of the HER catalyst (see below).

Figure 6 shows four TEM images of MoS₂ deposited on MWCNTs (diameters ranging from 20 to 40 nm) in transverse and longitudinal cross sections. As shown, MoS₂ nanosheets surround MWCNTs whereas S–Mo–S layer units appear as stacks of distinctive bold black lines on the MWCNT substrates. The carbon layers beneath are represented as black lines of lower intensity and thickness. Besides, the line distances can also be used to distinguish MoS₂ from the carbon substrate. Graphite like MWCNT has a lattice distance of around 3.4 Å while 2H-MoS₂ is characterized by a S–Mo–S layer distance of around 6.4 Å [10]. The MoS₂ nanosheets partially adapt to the bending of the carbon nanotubes, but in most cases the MoS₂ nanosheets show no bending and appear as individual flat MoS₂ nanosheets showing small extension of the (00.1) planes compared to the nanosheet thickness. This observation is consistent with the model that the

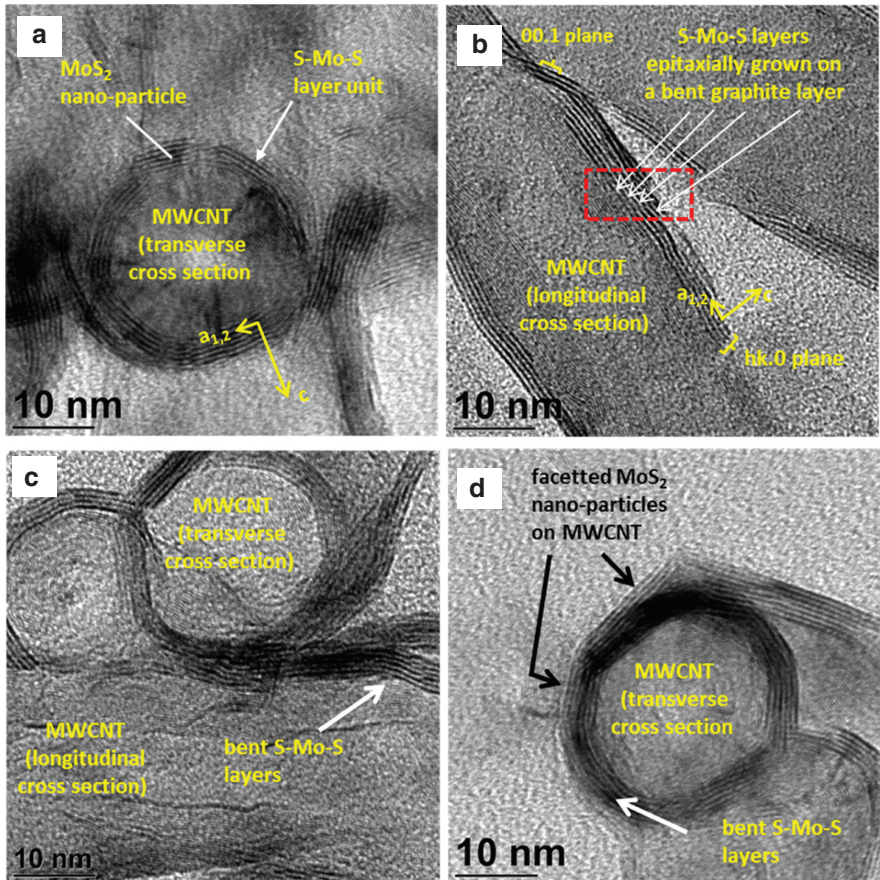


Fig. 6: TEM images of transverse and longitudinal cross sections of MWCNTs surrounded by S–Mo–S layer stacks. (a) Unbent S–Mo–S stacks with gaps between the particles with an extension of 5–10 nm, (b) slightly bent S–Mo–S units with a length <30 nm which are oriented parallel to carbon fibers, (c) faceted growth of MoS₂ nanoparticles enveloping a multiwall carbon nanofiber, (d) partly bent MoS₂ particles enveloping a carbon fiber.

bending behavior of MoS₂ is limited as shown schematically in Figure 7. As a consequence, MoS₂ nanosheets are separated from each other by a small gap with decreasing MWCNT diameter (see Figure 6a). The surfaces of the S–Mo–S layers are 10 nm–20 nm broad and at least 50 nm long, the S–Mo–S stack number varies from 1 to 7 layer units. Encapsulation of MWCNTs by stacks of S–Mo–S layers can be understood as a hexagonal cylinder enclosing the individual carbon nanotubes under ideal conditions. Ideally, the gaps between the individual nanosheets are expected to be large enough that protons in the electrolyte have access to the edges

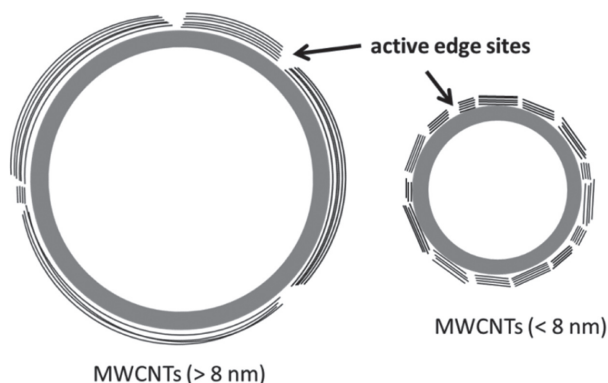


Fig. 7: Scheme of MoS₂ nanosheets grown on MWCNT substrates with different diameters.

of the S–Mo–S units. Best catalytic material is expected to have a high stacking number of S–Mo–S entities which then offer a large number of reactive sites at the particle electrolyte.

Figure 8a shows the catalytic activity of the MoS₂ grown on MWCNTs. As already explained in Figure 4, again a splitting of the curves between the forward and reverse scan due to capacitive effects can be seen. The capacitance corrected curves are shown in Figure S3. The sample deposited on the smallest diameter MWCNTs (<8 nm) obtained a current density of 2 mA/cm² at the potential of –0.3 V vs. RHE, which is the highest activity. The current densities of the other samples at the same potential are ranging from 1.4 to 1.0 mA/cm². The light grey

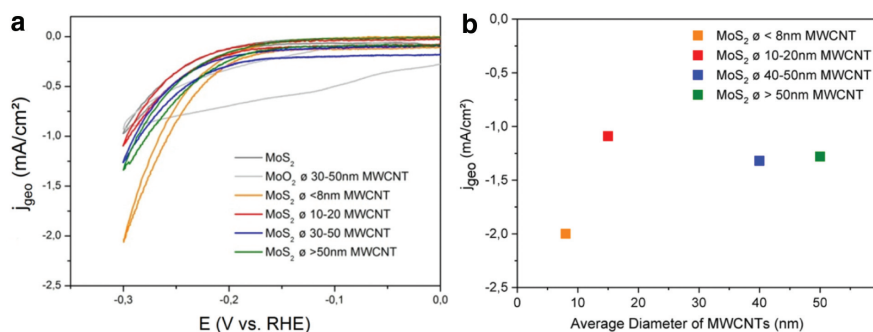


Fig. 8: (a) CV-curves of MWCNT supported MoS₂ nanoparticles in comparison to DS-315 and a pure MoO₂ electrode; data were measured in 0.5 M H₂SO₄ with a scan rate of 10 mV/s; the data were iR-corrected according to the procedure described in the experimental section; for C_{dl} corrected curves see Figure S3; (b) dependency of the current density at a voltage of –0.3 V vs. RHE as a function of the diameter of MWCNTs; data were taken from Figure 8 (a).

curve shows the CV curve of MoO_2 which proves that this phase has only a moderate catalytic activity. In neither the MoS_2 powders nor the MoS_2 layer sequences grown on the carbon MWCNTs, hydrogen sulfide evolution (H_2S) as a corrosion product has been detected investigating the released gases by a mass spectrometer coupled to our electrochemical cell. Figure 8b shows the current density as a function of the average diameter of MWCNTs at a potential of -0.3 V vs. RHE. As explained above (see Figure 4) at this highest applied potential the Faraday current has the highest contribution to the overall current density. The result is comparable to the dependence of the current density of MoS_2 powders on the particle size (see Figure 4b). In the case of MoS_2 deposited on MWCNTs of 8 nm diameter, the improved catalytic performance can be explained by a higher number of catalytic sites at the edges of S–Mo–S units owing to a higher number of stacks which are accessible by the electrolyte. To prove this assumption, clarification of the catalytic centers in different MoS_2 electrodes were investigated by electro-oxidation.

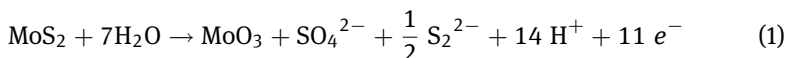
Since MoS_2 is highly anisotropic the question arises how far the electrical conductivity influences the catalytic behavior considering changes of the particle dimension and the orientation of the nanosheets with respect to the carbon nanotubes. It is known that bulk 2H- MoS_2 is a compound semiconductor with an indirect band gap of $E_g = 1.4$ eV followed by a direct one at $E_g = 1.9$ eV. In 1983, Thakurta and Dutta studied the specific conductance of highly doped natural crystals perpendicular (s_{\perp}) and parallel (s_{\parallel}) to the hexagonal c-axis [37]. They found a specific conductance for s_{\perp} ranging from 0.078 – 1.09 $\text{W}^{-1}\text{cm}^{-1}$ while s_{\parallel} was four orders of magnitude smaller ranging from 3.0 – 4.6×10^{-4} $\text{W}^{-1}\text{cm}^{-1}$. This means that the conductivity parallel to the hexagonal surface is high compared to the conductivity perpendicular to the hexagonal c-axis. Since the number of S–Mo–S is typically four to seven in our case (see Figure 6) electron transport from the carbon tubes via the stacked S–Mo–S layers to the catalytically active centers is small compared the conductivity in the S–Mo–S layers. This means that both particle dimension and number of stacks determine the transport velocity of electrons from the carbon nanotube via the MoS_2 nanosheets to the catalytically active centers. Since in our MWCNT supported MoS_2 catalyst nanoparticles the S–Mo–S stacking number did not change when lowering the particle extension of the 00.1 facets the number of edges is mainly determining the catalytic performance as will be discussed and demonstrated in the following chapter.

3.3 Clarification of the catalytic center by electro-oxidation

Bonde et al. [32] analyzed MoS_2 samples by a surface-sensitive method, X-ray photoelectron microscopy (XPS) before and after electro-oxidation. They could show

that the intensities of the Mo 3d and Mo 3p signals as well as the S 2s and S 2p decreased after the experiment. This can be explained by a number of reasons: a) MoS₂ could delaminate from the surface of the conductive support or b) MoS₂ is oxidized to MoO₃ (Mo³⁺) which could be soluble in the electrolyte. According to the work of n-type photoactive MoS₂ single crystals, sulfur compounds such as SO₄²⁻, S₂²⁻ and MoO₃ are formed after electrochemical measurements in potassium nitrate (KNO₃) [38].

The reaction equation of the oxidation at the edges can be expressed by the equation [32]:



According to the literature [9], the catalytically active centers of molybdenum disulfide are located at Mo atoms piercing out of hk.0 and h0.l surfaces of the crystalline material. Since the edge Mo atoms with dangling bonds and Mo atoms of complete coordination of sulfur sandwiched between sulfur layers (basal planes) have different electrochemical properties, the electro-oxidation of these two kinds of atoms should appear as two separate peaks in CV curves under anodic conditions. Therefore by electro-oxidation, the edges should be distinguishable from basal planes. This process could be verified by passivating the edges with a nonionic surfactant, e.g. Tween 80 as demonstrated in the following discussion.

In our study electro-oxidation is performed using MoS₂ nanosheets grown on MWCNTs. The edge-basal plane-ratio of the samples has been determined by electro-oxidation and the correlation between the current density and the edge-basal plane-ratio is discussed.

3.3.1 Passivation of the edges with Tween 80

By treating a HEC characterized by a layer structure with organic detergents, the CV characteristics can be influenced, since the detergents are specifically attaching to the reactive edges of the individual layer units. To investigate this behavior, organic detergents with ligands that act as electron donors and molecules with large functional groups, which affect and limit the reaction due to steric hindrance, are used. Chemical treatment of photocatalysts were first described by Parkinson et al. [39]. In their experiments, treatments with organic ligands such as 1,2-bis (diphenylphosphino) ethane (diphos), which is commonly used for rodium-catalyzed hydroformylation [40], showed a lower dark current and a higher open-circuit voltage. In the treatment of tungsten diselenide (WSe₂) single crystals, the phosphorous atom of the diphos reacts with tungsten atoms at

the edges or on steps of (00.1) facets of hexagonal crystals. Other ligands such as isocyanides, thiocarbamates [41], ethylenediamine tetraacetate (EDTA) [42], and 1,2-diaminobenzene (OPD) [43], also show a reduction of the dark current due to passivation of recombination centers on the (00.1) planes and crystal edges.

In this work, the nonionic surfactant Tween 80, which is used as an oil/water emulsifier [44], was chosen as passivation material. Tween 80 is an ethoxylated sorbitan fatty acid ester with the trade name Tween. The structure of Tween 80 is shown in Figure 9. The sorbitans differ in their fatty acid, the middle number of the polyoxyethylene units of the molecule, and the degree of esterification. In Tween 80, the number 8 stands for the oleic acid and number 0 stands for a monoester with 20 polyethylene units.

After the MoS₂ samples were impregnated with Tween 80, the influence of the surfactant on the catalytic activity has been investigated by electrochemical measurements. After treatment of MoS₂ with Tween 80, the surfactant covers the edges of the S–Mo–S slabs, which are considered as the reaction centers for the HER. This experiment can additionally clarify the meaning of the oxidation peaks in the CV curves shown below (Figure 11), which are attributed to an electro-oxidation of the catalyst.

Figure 10 shows the CV characteristic of a MoS₂ single crystal in the potential range from 0.6 V to –0.4 V vs. RHE with and without Tween 80. The initial cycle was measured up to a potential of 1.7 V vs. RHE to clean the surface. This effect is noticeable in Figure 10 by an increased current density in the following CV cycles as shown by the black arrow. The current density of the MoS₂ single crystal electrode after cleaning is about 0.5 mA/cm² at –0.4 V vs. RHE. After passivation of the active sites by Tween 80, the current density reduces to –0.05 mA/cm² at the same potential (orange curve in Figure 10). As the number of CV cycles increases, the current density in hydrogen evolution of the sample treated with Tween

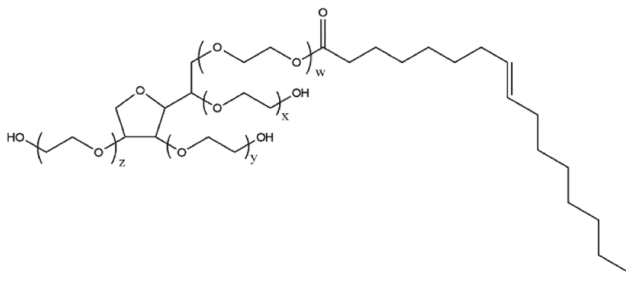


Fig. 9: Structure of the non-ionic surfactant Tween 80 ($w + x + y + z = 20$).

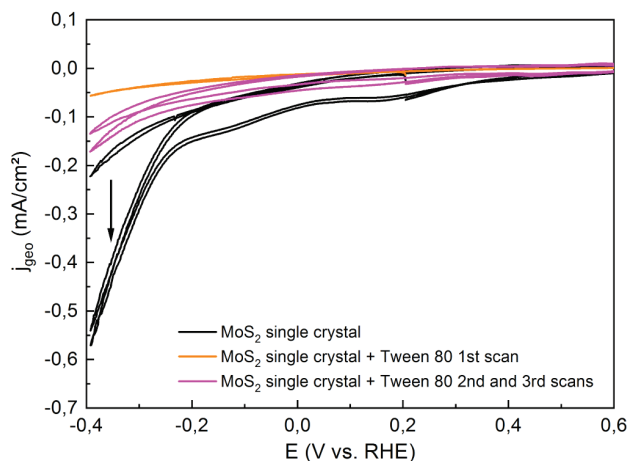


Fig. 10: CV curve of a MoS₂ single crystal before (black curve) and after impregnation with Tween 80 (orange and pink curves). All curves are iR-corrected as described in the experimental section.

80 increases as well. The surfactant is apparently reversibly coordinating the edges.

Figure 11a displays the CV curve of MoS₂ nanosheets grown on ARKM005 MWCNTs (diameter >50 nm) with and without Tween 80 taken in the positive potential range. The surfactant slightly also alters the second oxidation peak since the surfactant partially covers the (00.1) surfaces. However, the intensity of the first oxidation peak is significantly reduced after the treatment with Tween 80 and the peak position is shifted by about 50 mV (see Figure 11b). According to the CV of the electrode before and after the treatment with Tween 80 in Figure 11c, Tween 80 is obviously attached to the edge sites of S–Mo–S entities passivating the catalytically active centers because the current density at negative potential decreases dramatically, which was also found for the MoS₂ single crystal (see Figure 9). From the change of the two electro-oxidation peaks in Figure 11a, it can be concluded that the first electro-oxidation peak is connected with an oxidation of the edge sites while the second peak is correlated to the oxidation of the basal planes. Since the first peak is still visible after the treatment of Tween 80, only a part of the catalytically active centers was passivated by Tween 80. The reason could be that the surfactant has a large steric hindrance due to the presence of the polyoxoethylene group. Therefore, it is not able to coordinate to all metal atoms at the MoS₂ edges. This fact is also the reason why the evolution of hydrogen of the cathode does not completely disappear after Tween 80 treatment in Figure 11c.

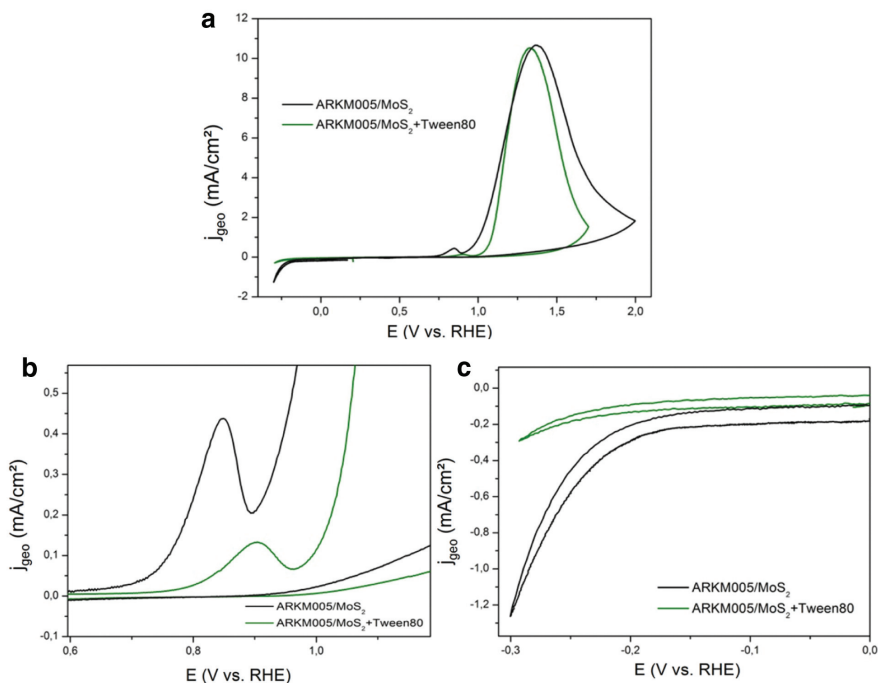


Fig. 11: Passivation of the edges of the S–Mo–S nanosheets of MoS₂ nano-particles deposited on MWCNTs (ARKM005 $\varnothing > 50$ nm) with Tween 80: (a) oxidation behavior at a glance: (b) oxidation behavior of the first peak before and after treatment with TWEEN 80 magnified and (c) HER behavior of the electrode before (black curve) and after treatment with TWEEN 80 (green curve). All curves are iR-corrected by the procedure described in the experimental section.

3.3.2 Electro-oxidation of MoS₂ nanosheets grown on MWCNTs with different diameters

Since the edges and basal planes in MoS₂ can be identified and also quantified by electro-oxidation, the catalytic properties of MoS₂ nanosheets grown on MWCNTs of different diameter were studied by CV. In this study, the correlations between the current density and the edge-to-basal-plane-ratio for MoS₂ nanosheets deposited on MWCNTs were determined.

Table 2 shows the calculated area of the first (A_1) and the second (A_2) electro-oxidation peak, respectively, as well as the edge-to-basal-plane ratio for different MWCNT/MoS₂ electrodes. According to Table 2, the four MWCNT/MoS₂ samples with different diameters have similar A_2 values, suggesting similar basal plane areas. However, the A_1 value of ARKM001/MoS₂ was significantly higher

Tab. 2: Calculation of peak areas and edge-to-basal plane-ratios of MoS₂ deposited on MWCNTs.

	1. Peak area A ₁ (Q, C/cm ²)	2. Peak area A ₂ (Q, C/cm ²)	Edge-to-basal plane-ratio A ₁ /A ₂ (%)
ARKM001/MoS ₂ Ø <8 nm	0.040	1.421	2.8
ARKM002/MoS ₂ 10–20 nm	0.013	1.292	1.0
ARKM004/MoS ₂ 40–50 nm	0.014	1.489	0.9
ARKM005/MoS ₂ Ø >50 nm	0.012	1.704	0.7

than in the other three samples. Therefore, this sample also obtains the highest edge-to-basal-plane-ratio.

In the following, the current densities of the MWCNT/MoS₂ electrodes were compared with the edge-to-basal-plane-ratios to further study the impact of these ratios on the catalytic property of samples. Figure 12a compares the obtained geometric current density with the edge-to-basal-plane ratio as a function of MWCNT

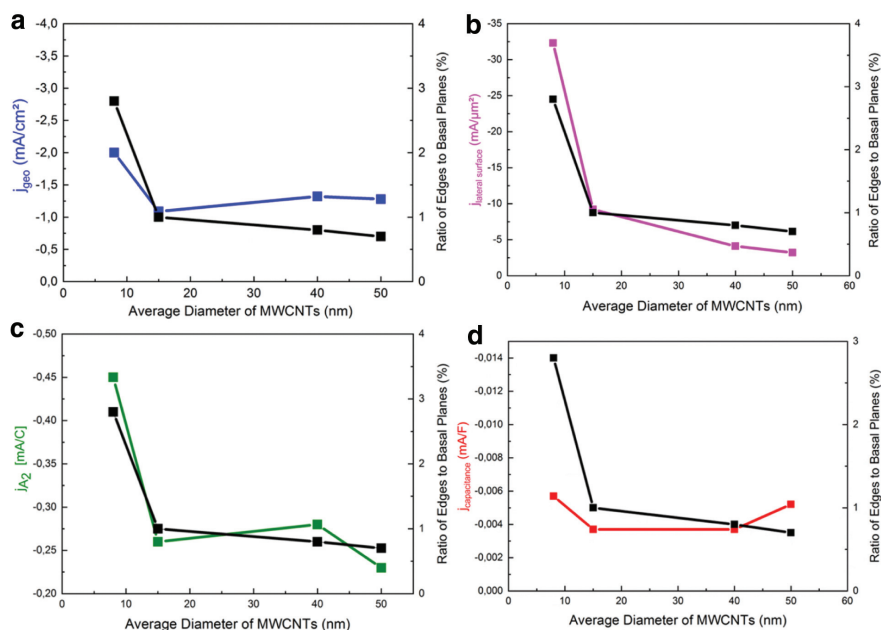


Fig. 12: Comparison the edge-area-ratio as a function of the MWCNTs' diameter with: (a) geometric current density, (b) current density divided by shell surface of the MWCNTs, (c) current density divided by the second peak area, (d) specific capacitance.

diameter. The sample with the smallest diameter shows the largest current density and the largest edge-to-basal-plane ratio. The left y-axis in Figure 12b visualizes the current divided by the geometric area of the MWCNTs. As expected, the trend of this geometric current density is also consistent with the edge-to-basal-plane ratio. Figure 12c shows the comparison between the current density divided by the area of the second electro-oxidation peak and edge-to-basal plane-ratio correlating well with each other. In Figure 12d, the comparison of the current density divided by the Helmholtz double layer capacitance (C_d) and the edge-to-basal-plane ratio is shown. The capacitance C_d is measured by CV in a potential region where no electrochemical reaction is occurring. In this region, the capacitive current is proportional to the scan rate (df/dt) according to Eq. 2. The unit of the capacitance is As/V or F (Farad) [45].

$$i_c = \frac{dQ}{Dt} = \frac{\delta Q}{\delta \varphi} \frac{d\varphi}{dt} = C_d \frac{d\varphi}{dt} \quad (2)$$

In this equation, i_c stands for the capacitive current, Q stands for the electric charge, t is the time, and f is the potential, C_d stands for the Helmholtz double layer capacitance. As shown in Figure 12d, the edge-to-basal-plane-area ratio and the current densities as a function of capacitance do not correlate, the current divided by capacitance remains constant. The reason could be that MWCNTs have a large electrochemical capacitance which overlays the material-specific capacitance of the MoS_2 .

From this comparison, one could speculate that the large edge-to-basal-plane ratio in sample ARKM001/ MoS_2 is the main reason for its high current density, which leads to a higher number of active sites at the catalyst surface. In summary, HER active MoS_2 catalysts should have a high edge-area to van-der-Waals-plane ratio and at the same time a large FWHM in the E_{2g}^1 Raman peaks.

4 Conclusion

Electrodes made from powders and nanosheets of the molybdenum sulfide phase 2H- MoS_2 have been investigated as hydrogen evolution catalysts under acidic conditions. The catalytic center was identified at the edges of the hexagonal particles. Powders with a diameter >200 nm and carbon-supported MoS_2 nanosheets were fixed using PEDOT:PSS on conductive glass substrates (FTO). MoS_2 nanosheet deposited chemically on MWCNTs of different diameters had sizes in the range from 3 to 5 nm (particle height in 00.1 direction) and from 10 to 50 nm (extension of basal planes surrounding MWCNTs in transversal and longitudinal direction). The hydrogen evolution reaction was studied as a function of particle size

and especially as a function of the edge-to-basal-plane-area ratios of MoS₂. MWCNTs of different diameters were tested as support to study their influence on the growth and defects of MoS₂ particles. Among all samples, the MoS₂ grown on MWCNTs with smallest diameter ($\varnothing < 8$ nm) obtained the highest catalytic activity (2 mA/cm² at -0.3 V vs. RHE). By electro-oxidation, the catalytically active edge atoms could be distinguished from the inert atoms on the basal planes. This effect is confirmed by the passivation of edge sites using Tween 80 as surfactant, which mainly protects edge atoms from electro-oxidation. From these measurements, the edge-to-basal-plane ratios in different MoS₂ samples could be determined. During the comparison of different electrodes, the sample with highest catalytic activity was found to have the highest edge-to-basal plane-ratio, which means that the high catalytic activity of this sample is due to the high number of active edge atoms on the catalyst non-van-der-Waals surfaces.

Acknowledgment: We like to thank Stefanie Bierwirth, Dipjyoti Das, Dr. Stephan Brunken, Dr. Klaus Ellmer and Karsten Harbauer for their support setting up our sputtering system and performing first electrochemical measurements to characterize hydrogen evolution catalysis using MoS_x electrodes under acidic conditions. S.F. thanks Dr. Ibrahim Ahmed (HZB) for fruitful discussions. The work became possible due to the continuous and generous financial support in the DFG Priority Program SPP 1613 *SolarH2* and by the German Federal Ministry of Education and Research (BMBF) in the project “H₂-NanoSolar” (contract no. # 03SF0353A). We gratefully acknowledge the work of the coordinators at the Technische Universität Darmstadt (*SolarH2*), Prof. Dr. Wolfram Jaegermann, Dr. Bernd Kaiser and Mrs. Leslie Frotscher.

Funding: Deutsche Forschungsgemeinschaft, Funder Id: <http://dx.doi.org/10.13039/501100001659>, Grant Number: FI 1524/4-2.

References

1. R. R. Chianelli, T. A. Pecoraro, T. R. Halbert, W. H. Pan, E. I. Stiefel, *J. Catal.* **86** (1984) 226.
2. H. Wang, L. L. Yu, Y. H. Lee, Y. M. Shi, A. Hsu, M. L. Chin, L. J. Li, M. Dubey, J. Kong, T. Palacios, *Nano Lett.* **12** (2012) 4674.
3. H. E. Sliney, *Tribol. Int.* **15** (1982) 303.
4. A. R. Beal, W. Y. Liang, J. C. Knights, *J. Phys. Part C Solid State Phys.* **5** (1972) 3540.
5. S. N. Shirodkar, U. V. Waghmare, *Phys. Rev. Lett.* **112** (2014) 157601.
6. D. Yang, S. J. Sandoval, W. M. R. Divigalpitiya, J. C. Irwin, R. F. Frindt, *Phys. Rev. B* **43** (1991) 12053.
7. L. Gmelin, *Handbuch der Anorganischen Chemie*, C. Winter, Heidelberg (1886).

8. H. Tributsch, *Phys. Chem. Chem. Phys.* **81** (1977) 361.
9. T. F. Jaramillo, K. P. Jorgensen, J. Bonde, J. H. Nielsen, S. Horch, I. Chorkendorff, *Science* **317** (2007) 100.
10. J. Kibsgaard, Z. Chen, B. N. Reinecke, T. F. Jaramillo, *Nat. Mater.* **11** (2012) 963.
11. D. Kiriya, P. Lobaccaro, H. Y. Nyein, P. Taheri, M. Hettick, H. Shiraki, C. M. Sutter-Fella, P. Zhao, W. Gao, R. Maboudian, J. W. Ager, A. Javey, *Nano Lett.* **16** (2016) 4047.
12. H. Li, C. Tsai, A. L. Koh, L. Cai, A. W. Contryman, A. H. Fragapane, J. Zhao, H. S. Han, H. C. Manoharan, F. Abild-Pedersen, J. K. Nørskov, X. Zheng, *Nat. Mater.* **15** (2016) 48.
13. T. F. Jaramillo, J. B. Jingdong Zhang, B.-L. Ooi, K. Andersson, J. Ulstrup, I. Chorkendorff, *J. Phys. Chem. C* **112** (2008) 17492.
14. J. Kibsgaard, T. F. Jaramillo, F. Besenbacher, *Nat. Chem.* **6** (2014) 248.
15. D. Merki, S. Fierro, H. Vrubel, X. Hu, *Chem. Sci.* **2** (2011) 1262.
16. J. D. Benck, Z. Chen, L. Y. Kuritzky, A. J. Forman, T. F. Jaramillo, *ACS Catal.* **2** (2012) 1916.
17. J. D. Benck, T. R. Hellstern, J. Kibsgaard, P. Chakthranont, T. F. Jaramillo, *ACS Catal.* **4** (2014) 3957.
18. H. Vrubel, D. Merki, X. Hu, *Energy Environ. Sci.* **5** (2012) 6136.
19. D. Merki, H. Vrubel, L. Rovelli, S. Fierro, X. Hu, *Chem. Sci.* **3** (2012) 2515.
20. L. R. L. Ting, Y. Deng, L. Ma, Y.-J. Zhang, A. A. Peterson, B. S. Yeo, *ACS Catal.* **6** (2016) 861.
21. P. D. Tran, T. V. Tran, M. Orio, S. Torelli, Q. D. Truong, K. Nayuki, Y. Sasaki, S. Y. Chiam, R. Yi, I. Honma, J. Barber, V. Artero, *Nat. Mater.* **15** (2016) 640.
22. F. Xi, P. Bogdanoff, K. Harbauer, P. Plate, C. Höhn, J. Rappich, B. Wang, X. Han, van de R. Krol, S. Fiechter, *ACS Catal.* **9** (2019) 2368.
23. M. A. Lukowski, A. S. Daniel, F. Meng, A. Forticaux, L. Li, S. Jin, *J. Am. Chem. Soc.* **135** (2013) 10274.
24. N. McDevitt, J. Bultman, J. Zabinski, *Appl. spectrosc.* **52** (1998) 1160.
25. C. Chang, S. Chan, *J. Catal.* **72** (1981) 139.
26. R. N. Bhattacharya, C. Y. Lee, F. H. Pollak, D. M. Schleich, *J. Non-Cryst. Solids* **91** (1987) 235.
27. Y.-H. Choi, J. Cho, A. M. Lunsford, A.-M. Hashimi, L. Fang, S. Banerjee, *J. Mater. Chem. A* **5** (2017) 5129.
28. Gitti L. R. T. Frey, Manyalibo J. Matthews, M. S. Dresselhaus, G. Dresselhaus, *Phys. Rev. B* **60** (1999) 2883.
29. H. J. Conley, B. Wang, J. I. Ziegler, R. F. Haglund Jr., S. T. Pantelides, K. I. Bolotin, *Nano Lett.* **13** (2013) 3626.
30. M. Guc, J. Andrade-Arvizu, I. Y. Ahmet, F. Oliva, M. Placidi, X. Alcobé, E. Saucedo, A. Pérez-Rodríguez, A. L. Johnson, V. Izquierdo-Roca, *Acta Mater.* **183** (2020) 1.
31. B. C. Windom, W. Sawyer, D. W. Hahn, *Tribol. Lett.* **42** (2011) 301.
32. J. Bonde, P. G. Moses, T. F. Jaramillo, J. K. Nørskov, I. Chorkendorff, *Faraday Discuss.* **140** (2008) 219.
33. D. Kong, H. Wang, J. J. Cha, M. Pasta, K. J. Koski, J. Yao, Y. Cui, *Nano Lett.* **13** (2013) 1341.
34. D. Y. Chung, S.-K. Park, Y.-H. Chung, S.-H. Yu, D.-H. Lim, N. Jung, H. C. Ham, H.-Y. Park, Y. Piao, S. J. Yoo, *Nanoscale* **6** (2014) 2131.
35. R. A. DiLeo, B. J. Landi, R. P. Raffaele, *J. Appl. Phys.* **101** (2007) 064307.
36. H. Nii, Y. Sumiyama, H. Nakagawa, A. Kunishige, *Appl. Phys. Express* **1** (2008) 064005.
37. S. R. G. Thakurta, Sa. K. Dutta, *J. Phys. Chem. Solids* **44** (1983) 407.
38. W. Jaegermann, D. Schmeisser, *Surf. Sci.* **165** (1986) 143.

39. B. A. Parkinson, T. E. Furtak, D. Canfield, K. K. Kam, G. Kline, *Faraday Discuss.* **70** (1980) 233.
40. C. P. Casey, E. L. Paulsen, E. W. Beuttenmueller, B. R. Proft, L. M. Petrovich, B. A. Matter, D. R. Powell, *J. Am. Chem. Soc.* **119** (1997) 11817.
41. G. Kline, K. Kam, D. Canfield, B. A. Parkinson, *Sol. Energy Mat.* **4** (1981) 301.
42. T. Sakata, E. Janata, W. Jaegermann, H. Tributsch, *J. Electrochem. Soc.* **133** (1986) 339.
43. H. S. White, H. D. Abruna, A. J. Bard, *J. Electrochem. Soc.* **129** (1982) 265.
44. O. Neumüller, H. Römpp, *Römpps Chemie-Lexikon*, Franckh, Stuttgart, ed 8, (1979–1988).
45. C. H. Hamann, W. Vielstich, *Elektrochemie*, Wiley-Vch, Weinheim (2005).

Supplementary material: The online version of this article offers supplementary material (<https://doi.org/10.1515/zpch-2019-1490>).